

# Denoiser-based projections for 2D super-resolution multi-reference alignment

Jonathan Shani, Tom Tirer, Raja Giryes, and Tamir Bendory

**Abstract**—We study the 2D super-resolution multi-reference alignment (SR-MRA) problem: estimating an image from its down-sampled, circularly translated, and noisy copies. The SR-MRA problem serves as a mathematical abstraction of the structure determination problem for biological molecules. Since the SR-MRA problem is ill-posed without prior knowledge, accurate image estimation relies on designing priors that well-describe the statistics of the images of interest. In this work, we build on recent advances in image processing, and harness the power of denoisers as priors for images. To estimate an image, we propose utilizing denoisers as projections and using them within two computational frameworks that we propose: projected expectation-maximization and projected method of moments. We provide an efficient GPU implementation, and demonstrate the effectiveness of these algorithms through extensive numerical experiments on a wide range of parameters and images.

respectively. Explicitly, each observation  $y_i \in \mathbb{R}^{L_{\text{low}} \times L_{\text{low}}}$  takes the form

$$y_i[n_1, n_2] = x[(n_1K - s_i^1) \bmod L_{\text{high}}, (n_2K - s_i^2) \bmod L_{\text{high}}] + \varepsilon_i[n_1, n_2], \quad (\text{I.2})$$

where  $n_1, n_2 = 0, \dots, L_{\text{low}} - 1$ , and  $K := \frac{L_{\text{high}}}{L_{\text{low}}}$  is assumed to be an integer. Our goal is to estimate  $x$  (the high resolution image) from  $N$  low-resolution observations  $y_1, \dots, y_N$ , when the translations  $s_1, \dots, s_N$  are unknown. Figure 1 shows few examples of observations generated according to (I.1) at different noise levels.

The SR-MRA model, first studied for 1-D signals [2], is a special case of the multi-reference alignment (MRA) model: The problem of estimating a signal from its noisy copies, each acted upon by a random element of some group; see for example [3]–[8]. The MRA model is mainly motivated by single-particle cryo-electron microscopy (cryo-EM) technology: an increasingly popular technique to construct 3-D molecular structures [9]. In Section VI, we introduce the mathematical model of cryo-EM in detail and discuss how the techniques proposed in this paper have the potential to make a significant impact on the molecular reconstruction problem of cryo-EM. The MRA model is also motivated by a variety of additional applications in biology [10], [11], robotics [12], radar [13], [14], and image processing [15], [16].

Previous works on MRA mostly focused on two computational frameworks: the method of moments (MoM) and expectation-maximization (EM); see for example [5], [6]. They are currently considered the leading techniques for solving MRA problems. MoM is a classical parameter estimation technique, aiming to recover the parameters of interest (e.g., signal, image, 3-D molecular structure) from the moments of observed data. MoM requires a single pass over the observations, making it an efficient technique for large data sets (large  $N$ ). Nevertheless, MoM is not statistically efficient. The EM algorithm aims to maximize the likelihood function (or the posterior distribution in a Bayesian framework) [17]. While each EM step does not decrease the likelihood

## I. INTRODUCTION

The 2D super-resolution multi-reference alignment (SR-MRA) problem entails estimating an image  $x \in \mathbb{R}^{L_{\text{high}} \times L_{\text{high}}}$  from its  $N$  circularly-translated, down-sampled, noisy copies:

$$y_i = PR_{s_i}x + \varepsilon_i, \quad i = 1, \dots, N, \quad (\text{I.1})$$

where  $R_s$  denotes a 2D circular translation,  $P$  denotes a down-sampling operator that collects  $L_{\text{low}} \times L_{\text{low}}$  equally-spaced samples of  $R_sx$ , and  $\varepsilon_i \in \mathbb{R}^{L_{\text{low}} \times L_{\text{low}}}$  is a noise matrix whose entries are drawn i.i.d. from  $\mathcal{N}(0, \sigma^2)$ . To ease exposition, we consider only square images, but the model can be easily extended to non-square images as well. The 2D translation  $s$  is composed of a horizontal translation  $s^1$  and a vertical translation  $s^2$ , which are drawn i.i.d. from unknown distributions,  $\rho_1$  and  $\rho_2$ ,

J.S., R.G., and T.B. are with the Department of Electrical Engineering, Tel Aviv University. T.T. is with the Faculty of Engineering, Bar-Ilan University. T.B. is partially supported by the BSF grant no. 2020159, NSF-BSF grant no. 2019752, and ISF grant no. 1924/21. R.G. is partially supported by the ERC-StG (No. 757497) grant.

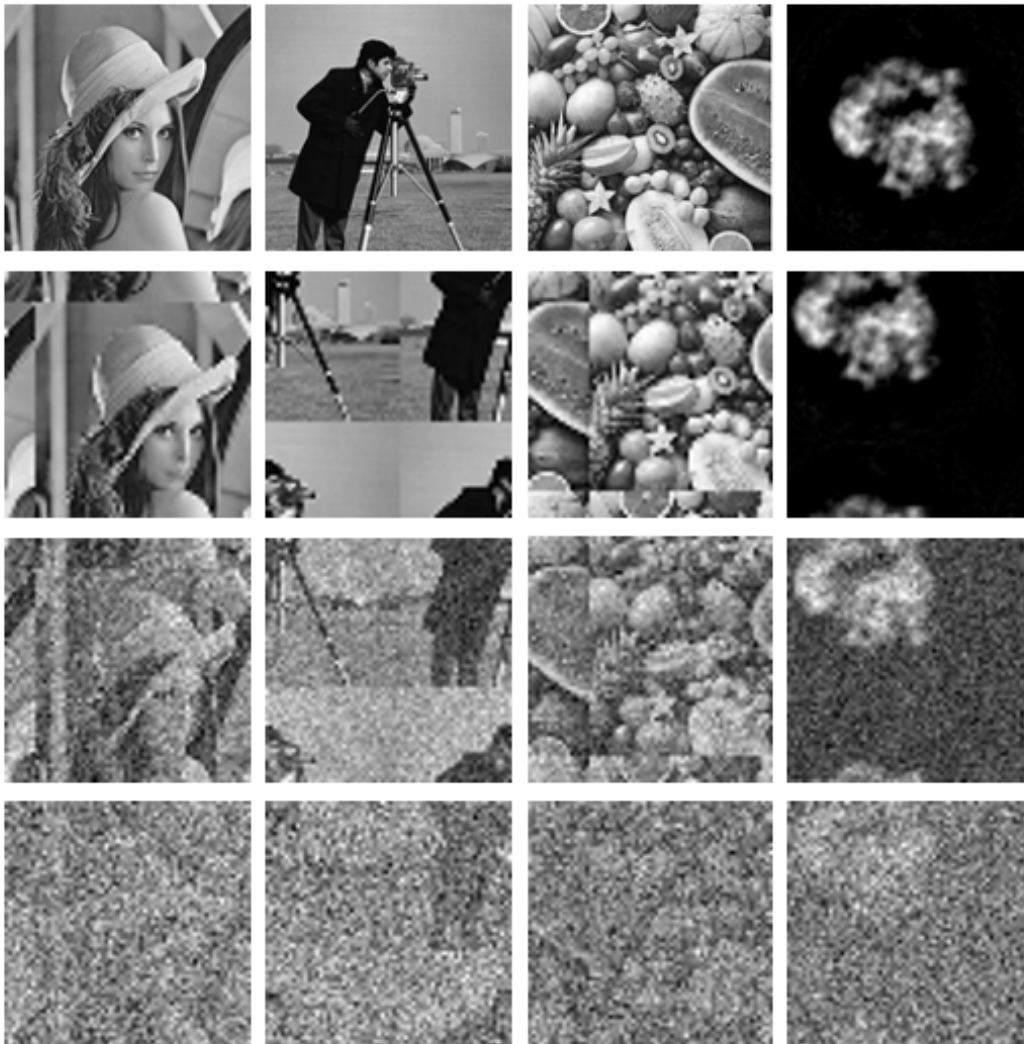


Fig. 1. Examples of observations generated according to model (I.1). The upper row shows 4 images of size  $128 \times 128$ . The second row shows the images after a 2D circular translation and down-sampling by a factor of  $K = 2$  to size  $64 \times 64$ . The third and fourth rows present observations in a low noise regime of  $\sigma = 1/8$  and a medium noise regime of  $\sigma = 1/2$ , respectively. The fourth column depicts a cryo-electron microscopy image of an E. coli 70S ribosome, available at the Electron Microscopy Data Bank [1].

function, it is not guaranteed to achieve the maximum of the likelihood function of (I.1) due to its non-convexity. Section II provides the necessary background for this paper, including an introduction to both methods.

As we will prove in Section II-A, it is impossible to uniquely identify the image  $x$  only from the SR-MRA observations (I.1), regardless of the specific estimation algorithm, as there are many different images that result in the same likelihood function. Therefore, to estimate the image accurately, it is necessary to incorporate a prior. Incorporating a prior into MoM and EM, and its application to SR-MRA, is the main focus of this paper.

In this work, we harness a recent line of works that use denoisers as priors. Utilizing existing state-of-the-art denoisers has been originally proposed as

part of the Plug-and-Play technique [18]. The Plug-and-Play method and its variants have been proven highly effective for many imaging inverse problems; see for example [19]–[35]. Essentially, the underlying idea is exploiting the impressive capabilities of existing denoising algorithms in order to replace explicit, traditional priors. Indeed, these techniques are especially useful for natural images, whose statistics are too complicated to be described explicitly, but for which excellent denoisers have been devised.

Our proposed computational framework, presented in Section III, uses denoisers as projection operators. Specifically, every few iterations of either MoM or EM, we apply a denoiser to the current estimate. This stage can be interpreted as projecting the image estimate

onto the implicit space spanned by the denoiser. In contrast to Plug-and-Play, our technique requires minor modifications to existing algorithms. Moreover, we found that this strategy led to better results than Plug-and-Play in the SR-MRA setting. In Section IV we provide convergence analysis for the projected MoM under a proximity assumption on the denoiser. We also present a more general operator-based analysis that, under suitable assumptions, provides mathematical reasoning for the convergence of non-gradient based algorithms, such as projected EM. Section V demonstrates the effectiveness of the method by extensive numerical experiments on natural and cryo-EM images. Section VI concludes the paper by discussing how our framework can be modified to other statistical models, and in particular to recover molecular structures using cryo-EM.

## II. BACKGROUND

Before introducing our proposed framework, we elaborate on the four pillars of this work: the non-uniqueness of the SR-MRA model (I.1), MoM, EM, and denoiser-based priors. Hereafter, we let  $\rho := [\rho_1, \rho_2]^T$ , and define the set of sought parameters as  $\theta := (x, \rho) = (x, \rho_1, \rho_2)$ . With a slight abuse of notation, we treat the image  $x$  and a measurement  $y_i$  as vectors in  $\mathbb{R}^{L_{\text{high}}}$  and  $\mathbb{R}^{L_{\text{low}}}$ , respectively. We also define  $\Theta = \mathbb{R}^{L_{\text{high}}^2} \times \Delta_{L_{\text{high}}} \times \Delta_{L_{\text{high}}}$ , where  $\Delta_{L_{\text{high}}}$  is the  $L_{\text{high}}$ -dimensional simplex, so that  $\theta \in \Theta$ .

### A. SR-MRA observations do not identify the image $x$ uniquely

The following theorem states that the likelihood function of (I.1) does not determine the image  $x$  uniquely. This in turn implies that a prior is necessary for accurate estimation of the sought image.

**Theorem II.1.** *The likelihood function  $p(y_1, \dots, y_N | x, \rho)$  does not determine uniquely the sought parameters  $x$  and  $\rho$ .*

*Proof.* The proof follows the guidelines of the proof of [2, Theorem 3.1]. Recall that  $y = PR_s x + \varepsilon$ , and that  $K := \frac{L_{\text{high}}}{L_{\text{low}}}$  is an integer. Let us define a set of  $K^2$  sub-images, indexed by  $n_1, n_2 = 0, \dots, K - 1$ :

$$x_{n_1, n_2}[\ell_1, \ell_2] := x[n_1 + \ell_1 K, n_2 + \ell_2 K],$$

for  $\ell_1, \ell_2 = 0, \dots, L_{\text{low}} - 1$ . Then, the SR-MRA model can be equivalently written as

$$y = R_t x_{n_1, n_2} + \varepsilon, \quad (\text{II.1})$$

where  $R_t$  is a translation over the low-resolution grid of size  $L_{\text{low}} \times L_{\text{low}}$  (in contrast to  $R_s$  in (I.1), which is a

translation over  $L_{\text{high}} \times L_{\text{high}}$ ). We denote the distribution of choosing the sub-image  $x_{n_1, n_2}$  and translating it by  $t$  as  $\rho[n_1, n_2, t]$ . Thus, the likelihood function of (I.1), for a single observation  $y$ , can be written, up to a constant, as

$$p(y; x, \rho) = \sum_{n_1, n_2=0}^{K-1} \sum_t \rho[n_1, n_2, t] e^{-\frac{1}{2\sigma^2} \|y - R_t x_{n_1, n_2}\|_2^2}. \quad (\text{II.2})$$

It is readily seen that the likelihood function is invariant under any permutation of the sub-images (over all  $K^2!$  permutations), and under any translation of each of them (overall  $(L_{\text{low}}^2)^{K^2}$  possible translations). This implies that there are  $K^2!(L_{\text{low}}^2)^{K^2}$  different images with the same likelihood function  $\square$

Figure 2 compares recoveries of the images presented in Figure 1 using the projected MoM and the projected EM, which are our proposed algorithms and are discussed in Section III. Specifically, the first and third rows show recoveries using Algorithm 1 and Algorithm 2, respectively, while the second and fourth rows show the outputs of the standard MoM and EM, with no prior. Evidently, in light of Theorem II.1, the latter results are of low quality.

### B. The method of moments (MoM)

MoM aims to estimate the parameters of interest (in our case, the image  $x$  and the distribution  $\rho$ ) from the observable moments. Recall that the  $d$ th observable moment is given by

$$\hat{M}_d := \frac{1}{N} \sum_{i=1}^N y_i^{\otimes d}, \quad (\text{II.3})$$

where  $y^{\otimes d}$  is a tensor with  $(L_{\text{low}}^2)^d$  entries. Computing the observable moments requires a single pass over the data and results in a concise summary of the data. By the law of large numbers, for sufficiently large  $N$ , we have

$$\hat{M}_d \approx \mathbb{E} y^{\otimes d} := M_d(\theta), \quad (\text{II.4})$$

where the expectation is taken against the distribution of the translations and the noise. Finding the optimal parameters  $\theta$  that fit the observable moments is usually performed by minimizing a least squares objective as a function of the parameters  $\theta$ :

$$\min_{\theta \in \Theta} \sum_{d=1}^D \lambda_d \|\hat{M}_d - M_d(\theta)\|^2, \quad (\text{II.5})$$

for some predefined weights  $\lambda_1, \dots, \lambda_D$  [36].

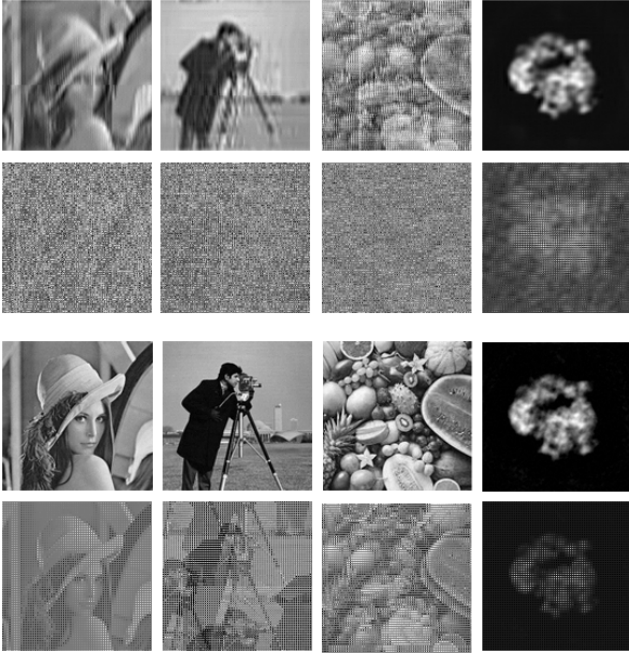


Fig. 2. The first and third rows present recoveries using the projected MoM and projected EM, outlined in Algorithm 1 and Algorithm 2, respectively. The second and fourth rows present recoveries using MoM and EM, without projection. As Theorem II.1 indicates, the projection (or alternative prior information on the sought image) is vital for accurate recovery. The experiment was conducted on images of size  $L_{\text{high}} = 128$  with a down-sampling factor of  $K = 2$ . MoM used the exact moments (corresponding to  $N \rightarrow \infty$ ), and the noise level and number of observations for the EM was  $\sigma = 1/8$  and  $N = 10^4$ , respectively. For the projected algorithms, we set  $F = 5$  (a detailed explanation is given in Section III).

Model (I.1) was studied in [6] when  $P$  is identity (no down-sampling)<sup>1</sup>. In particular, it was shown that if the discrete Fourier transform of the signal is non-vanishing, and  $\rho$  is almost any non-uniform distribution, then the signal and distribution are determined uniquely, up to an unavoidable translation symmetry, from the second moment of the observations. While this is not necessarily true when  $P$  is a down-sampling operator, we keep using the first two moments in this work (namely,  $D = 2$ ).

Specifically, the first two moments of the SR-MRA model (I.1) are given by [36]:

$$M_1 = PC_x \rho, \quad (\text{II.6})$$

$$M_2 = PC_x D_\rho C_x^T P^T + \sigma^2 P P^T, \quad (\text{II.7})$$

where  $C_x \in \mathbb{R}^{L_{\text{high}}^2 \times L_{\text{high}}^2}$  is a block circulant with circulant

blocks (BCCB) matrix of the form:

$$C_x = \begin{pmatrix} c_0 & c_{L_{\text{high}}-1} & \dots & c_2 & c_1 \\ c_1 & c_0 & c_{L_{\text{high}}-1} & \dots & c_2 \\ \dots & \dots & \dots & \dots & \dots \\ \dots & \dots & \dots & \dots & \dots \\ c_{L_{\text{high}}-1} & c_{L_{\text{high}}-2} & \dots & c_1 & c_0 \end{pmatrix}, \quad (\text{II.8})$$

where the block  $c_i \in \mathbb{R}^{L_{\text{high}} \times L_{\text{high}}}$  represents a circulant matrix of the  $i$ th column of the image  $x$  (as an image, not as a vector). Each column of  $C_x$  contains a copy of the image after 2D translation and vectorization. The matrix  $D_\rho \in \mathbb{R}^{L_{\text{high}}^2 \times L_{\text{high}}^2}$  is a diagonal matrix, whose diagonal is a vectorization of the matrix  $\rho_1 \rho_2^T$ . Therefore, the least squares objective (II.5) can be explicitly written as

$$\min_{\theta \in \Theta} \|PC_x D_\rho C_x^T P^T + \sigma^2 P P^T - \hat{M}_2\|_F^2 + \lambda \|PC_\rho x - \hat{M}_1\|_2^2. \quad (\text{II.9})$$

In this paper, we set  $\lambda = \frac{1}{L_{\text{high}}^2(1+\sigma^2)}$ , as suggested in [6].

We note that while the maximum likelihood estimator is asymptotically efficient (under mild conditions), MoM is not an efficient estimator. In addition, the objective function (II.9) consists of polynomials of degree 4 (in  $x$ ) and thus is non-convex. Therefore, we are not guaranteed to find its global minimizer. Nevertheless, our numerical experiments in Section V reveal that, when using denoiser-based projections, minimizing (II.9) using a standard gradient-based algorithm leads to accurate recoveries.

### C. Expectation-maximization (EM)

The log-likelihood of (I.1), up to a constant, is

$$\log p(y_1, \dots, y_n; \theta) = \sum_{i=1}^N \log \sum_{s^1, s^2=1}^{L_{\text{high}}} \rho[s] e^{-\frac{1}{2\sigma^2} \|y_i - P R_s x\|_2^2}, \quad (\text{II.10})$$

where we remind the reader that  $s = [s^1, s^2]^T$ . We note that this is a special case of the Gaussian mixture model, where all centers are connected through the group action (i.e., a translation). A popular way to maximize the likelihood function is using the EM algorithm [17]. EM can also be used to maximize the posterior distribution (rather than the likelihood function) when an analytical prior is available. EM has been proven effective in many practical scenarios, including for processing cryo-EM experimental datasets [37], [38].

EM is an iterative algorithm, where each iteration consists of two steps. In the first step, called the E-step, we compute the expected value of the log-likelihood function with respect to the translations, given the current

<sup>1</sup>The results of [6] concern 1-D signals, but they can be readily extended to 2D.

estimate of  $\theta := (x, \rho)$ . In the  $(t+1)$ -th iteration, it reads

$$Q(x, \rho | x_t, \rho_t) = \sum_{i=1}^N \sum_{s^1, s^2=1}^{L_{\text{high}}} w_t^{i,s} \left( \log \rho[s] - \frac{1}{2\sigma^2} \|y_i - PR_s x\|_F^2 \right), \quad (\text{II.11})$$

where

$$w_t^{i,s} = C_t^i \rho_t[s] e^{-\frac{1}{2\sigma^2} \|y_i - PR_s x\|_F^2}, \quad (\text{II.12})$$

and  $C_t^i$  is a normalization factor so that  $\sum_s w_t^{i,s} = 1$ . The next step, called the M-step, maximizes (II.11) with respect to  $x$  and  $\rho$ :

$$(x_{t+1}, \rho_{t+1}) = \underset{x, \rho}{\operatorname{argmax}} Q(x, \rho | x_t, \rho_t). \quad (\text{II.13})$$

In our case, the maximum is attained by solving the linear system of equations:

$$Ax_{t+1} = b, \quad (\text{II.14})$$

where

$$\begin{aligned} A &= \sum_{i=1}^N \sum_s w_t^{i,s} R_s^{-1} P^{-1} P R_s, \\ b &= \sum_{i=1}^N \sum_s w_t^{i,s} R_s^{-1} P^{-1} y_i, \\ \rho_{t+1}[s] &= \frac{\sum_{i=1}^N w_k^{i,s}}{\sum_{i=1}^N \sum_{s'} w_k^{i,s'}}. \end{aligned} \quad (\text{II.15})$$

The EM algorithm iterates between the E and M steps. While each EM iteration does not decrease the likelihood, for the SR-MRA model the likelihood function is not convex, and thus the EM algorithm is not guaranteed to achieve its maximum. A common practice to improve estimation accuracy is either to initialize the EM iterations in the vicinity of the solution (if such an initial estimate is available) or to run it multiple times from different initializations, and choose the estimate corresponding to the maximal likelihood value. As we show in Section V, our projected EM algorithm (described in the next section) provides consistent results even with a single initialization.

#### D. Plug-and-Play and denoiser-based priors

Using denoisers as priors was first proposed as part of the Plug-and-Play approach [18]. This strategy aims to maximize a posterior distribution  $p(\theta | y_1, \dots, y_n)$ , which is equivalent to the optimization problem:

$$\underset{\theta \in \Theta}{\operatorname{argmin}} l(\theta) + s(\theta), \quad (\text{II.16})$$

where  $l(\theta) := -\log p(y_1, \dots, y_n | \theta)$ ,  $s(\theta) := -\log p(\theta)$ ,  $p(\theta)$  is a prior on  $\theta$ , and recall that  $\theta = (x, \rho)$ . This work only considers a prior on the image  $x$ , but a prior on the distribution might be learned as well using the technique proposed in [39].

Plug-and-Play proceeds by variable splitting

$$\underset{\theta, v \in \Theta}{\operatorname{argmin}} l(x) + \beta s(v) \quad \text{subject to} \quad \theta = v, \quad (\text{II.17})$$

where  $\beta$  is a Lagrangian multiplier, which in practice can be tuned. This problem in (II.17) can be solved using ADMM by iteratively applying the following three steps:

$$\begin{aligned} \theta^{k+1} &= \underset{\theta \in \Theta}{\operatorname{argmin}} l(\theta) + \frac{\lambda}{2} \|\theta - (v^k - u^k)\|_2^2, \\ v^{k+1} &= \underset{v \in \Theta}{\operatorname{argmin}} \frac{\lambda}{2\beta} \|\theta^{k+1} + u^k - v\|_2^2 + s(v), \\ u^{k+1} &= u^k + (\theta^{k+1} - v^{k+1}). \end{aligned} \quad (\text{II.18})$$

The main insight here is that the second step aims to solve a Gaussian denoising problem, with a prior  $s(v)$  and noise level (standard deviation) of  $\sqrt{\frac{\beta}{\lambda}}$ . Instead of solving this problem with respect to an analytical explicit prior, it was suggested in [18] to apply empirical denoisers that have been developed over the years, such as BM3D or data-driven neural networks.

While Plug-and-Play provides impressive results in many image processing tasks, it requires tuning the hyper parameters  $\lambda, \beta$  and the number of iterations for the first step; these parameters have a significant impact on its performance. In particular, for our setup, we did not find a set of parameters that yields accurate estimates for the SR-MRA problem in a wide range of scenarios. As an alternative, in the next section we describe how denoisers can be used as projectors for EM and MoM.

### III. DENOISER-BASED PROJECTED ALGORITHMS

This section introduces the main contribution of this work: incorporating a projection-based denoiser into MoM and EM, and their implementation for SR-MRA. Importantly, there is no agreed way of including a prior into MoM, nor do we have a standard way of incorporating natural images prior to EM. The projected MoM algorithm is presented in Algorithm 1, and the projected EM is presented in Algorithm 2. The numerical experiments are deferred to Section V.

The main idea of our approach is rather simple: every few iterations of either MoM or EM, we apply a predefined denoiser that acts on the current estimate of the image. Specifically, for MoM, we apply the denoiser every few steps of BFGS (with line-search) that minimizes the least squares objective (II.9); BFGS can

be replaced by alternative gradient-based algorithms. For EM, we apply the denoiser every few EM steps.

As a denoiser, we chose to work with the celebrated BM3D denoiser [40] because of its simplicity and effectiveness for denoising natural images. However, replacing BM3D with alternative denoisers is straightforward. This might be especially relevant when dealing with specific applications, where a data-driven deep neural net may take the role of the denoiser. In Section VI, we discuss such potential applications to cryo-EM data processing.

Our algorithm requires only two parameters to be adjusted. The first parameter is the noise level of the denoiser, denoted hereafter by  $\sigma^{\text{BM3D}}$ . Low noise level increases the weight of the data (either likelihood or observed moments), while increasing the noise level strengthens the effect of the denoiser. In particular, we found that starting from a high noise level and gradually decreasing it with iterations leads to consistent and accurate estimations. Specifically, in the numerical experiments of Section V, we set the noise level to be

$$\sigma_t^{\text{BM3D}} = 2^{-1/10} \sigma_{t-1}^{\text{BM3D}}, \quad \sigma_1^{\text{BM3D}} = 1, \quad (\text{III.1})$$

where  $\sigma_t^{\text{BM3D}}$  is the noise level of the  $t$ th application of the BM3D denoiser.

The second parameter, which we denote by  $F$ , determines the number of EM iterations or BFGS iterations (or other gradient-based algorithm) for MoM between consecutive applications of the denoiser. Small or large  $F$  may put too much or too little weight on the prior (rather than on the data). Empirically, the projected MoM is quite sensitive to this parameter and requires carefully tuning  $F$ , as presented in Section V-E, whereas EM is less sensitive. In contrast to Plug-and-Play (see II-D), we found it to be quite easy to tune these two parameters and get consistent results for a wide range of images and parameters. The simplicity of parameter tuning, perhaps, stems from the fact that each parameter affects only one term ( $F$  the fidelity, and  $\sigma^{\text{BM3D}}$  the prior), whereas tuning the  $\lambda$  parameter in the Plug-and-Play approach (II.18) affects both terms.

#### IV. CONVERGENCE ANALYSIS

In this section, we present convergence analysis for the proposed algorithms. We start with a couple of definitions and assumptions that will be used throughout the analysis. Then, we provide convergence analysis for the projected MoM in a somewhat modified scheme, where the (nonconvex) MoM objective is reduced by a gradient descent step rather than BFGS iterations (which are essentially preconditioned gradient steps).

---

#### Algorithm 1: Projected MoM

---

**Input:** Measurements  $y_1, \dots, y_N$ , denoiser  $\mathcal{D}$ , and the parameter  $F$

**Output:** An estimate of  $\theta := (x, \rho)$  of the image and the distribution

- 1) Compute the empirical moments  $\hat{M}_1, \hat{M}_2$  according to (II.3)
  - 2) Until a stopping criterion is met:
    - a) Run  $F$  BFGS (or alternative gradient-based algorithm) steps to minimize (II.9)
    - b) Apply the denoiser  $x \leftarrow \mathcal{D}(x, \sigma^{\text{BM3D}})$
    - c) Update  $\sigma^{\text{BM3D}}$  according to (III.1)
- 

---

#### Algorithm 2: Projected EM

---

**Input:** Measurements  $y_1, \dots, y_N$ , denoiser  $\mathcal{D}$ , and the parameter  $F$

**Output:** An estimate of  $\theta := (x, \rho)$  of the image and the distribution

Until a stopping criterion is met:

- 1) Run  $F$  EM steps according to (II.12), (II.14), and (II.15).
  - 2) Apply the denoiser  $x \leftarrow \mathcal{D}(x, \sigma^{\text{BM3D}})$
  - 3) Update  $\sigma^{\text{BM3D}}$  according to (III.1)
- 

Lastly, to tackle frameworks that are not based on any gradient method, we present a more general operator-based analysis. While some assumptions in this analysis are not guaranteed for EM, it does provide mathematical reasoning for the convergence of frameworks that are composed of two “black-box” operators that generate convergent sequences, each on its own, which is relevant to EM.

Let us start with some definitions.

**Definition IV.1.** We say that the map  $\mathcal{M} : \mathcal{X} \rightarrow \mathcal{X}$  is  $C$ -Lipschitz in  $\mathcal{X}$  if for all  $x, z \in \mathcal{X}$  we have

$$\|\mathcal{M}(x) - \mathcal{M}(z)\|_2 \leq C\|x - z\|_2.$$

In particular, if  $C = 1$  then  $\mathcal{M}$  is nonexpansive in  $\mathcal{X}$  and if  $C < 1$  then  $\mathcal{M}$  is a contraction in  $\mathcal{X}$ .

**Definition IV.2.** The proximal operator associated with a function  $s(\cdot)$  is defined by

$$\text{Prox}_s(x) := \underset{z}{\operatorname{argmin}} \frac{1}{2}\|x - z\|_2^2 + s(z).$$

Observe the tight connection between the proximal operator and Gaussian denoising. Specifically, Gaussian denoiser  $\mathcal{D}(\cdot; \sigma)$  that is associated (perhaps implicitly) with a prior function  $s(\cdot)$  is typically obtained by an optimization problem similar to  $\text{Prox}_{\sigma^2 s}(x)$ .

The proximal operator has been originally explored under the assumption that  $s$  is a lower semi-continuous (l.s.c.) convex function [41], for which it has been shown that: 1) it is a subdifferential of a convex function and 2) it is 1-Lipschitz, i.e., nonexpansive. These properties are important for guaranteeing convergence of algorithms that use it. A recent work [42] has extended the analysis to nonconvex  $s$  (which may be more similar to practical denoisers), but these results do not imply nonexpansiveness without additional assumptions on the proximal operator. Thus, since the focus of the paper is on the data-terms (namely, the log-likelihood and the MoM objectives), we state our results for the case where  $\mathcal{D}$  is a proximal operator associated with a convex function.

The two iterative estimation schemes in this paper can be expressed as  $x_{k+1} = \mathcal{D}(\mathcal{T}(x_k))$ , where the denoiser  $\mathcal{D}$  follows an operation  $\mathcal{T}$  that reduces some nonconvex data-fidelity term: the first scheme reduces the MoM objective with a gradient-based method and the second scheme reduces the negative log-likelihood via the EM method. Note that both objectives are nonconvex even in the case that  $\rho$  is known or fixed. Therefore, for simplification, we assume in this section that  $\rho$  is fixed.

#### A. Convergence of projected MoM

Under the stated assumptions, let us provide convergence results for the iterative scheme

$$x_{k+1} = \mathcal{D}(x_k - \mu \nabla f(x_k)), \quad (\text{IV.1})$$

where  $f$  denotes the MoM objective with a fixed  $\rho$ , and  $\mu$  is the step-size. Notice that  $f$  is smooth but nonconvex. Compared to Algorithm 1, the main difference is merely replacing the BFGS steps with a gradient step.

To establish a convergence statement for (IV.1), we will exploit convergence results of the proximal gradient method from [43], [44]. To use these results, we need to show that the MoM is “smooth enough”—namely, has a Lipschitz gradient. Accordingly, the following theorem is based on proving that the gradient is Lipschitz when the optimization is restricted to a closed domain  $\mathcal{X}$ . This assumption is reasonable when  $x$  is an image, as typically its pixels are restricted to the range  $[0, 255]$ .

**Theorem IV.3.** *Consider the nonconvex MoM objective*

$$f(x) = \|PC_x D_\rho C_x^T P^T + \sigma^2 P P^T - \hat{M}_2\|_F^2 + \lambda \|PC_\rho x - \hat{M}_1\|_2^2, \quad (\text{IV.2})$$

with fixed  $\rho$  and domain  $\mathcal{X}$  that is a closed convex set. Let  $\mathcal{D} = \text{Prox}_{\mu s}$ , where  $s(\cdot)$  is a proper l.s.c. convex function with domain  $\mathcal{X}$ . Then, there exists  $\mu > 0$  such that the sequence  $\{x_k\}$  in (IV.1) converges to a fixed

point  $x_* = \mathcal{D}(x_* - \mu \nabla f(x_*))$ , which is a stationary point of  $f + s$ .

*Proof.* We need to show that, restricted to  $\mathcal{X}$ ,  $\nabla f$  is  $C$ -Lipschitz. Then by setting  $\mu \in (0, \frac{2}{C})$  the convergence to critical point follows from [44, Theorem 10.15].

Note that  $f(x)$  is infinitely differentiable. The Lagrange remainder (consequence of mean value theorem) of first order Taylor’s series of  $\nabla f$  implies that for any  $x, z \in \mathcal{X}$  there exists  $\xi$  on the line that connects  $x$  and  $z$  for which  $\nabla f(x) = \nabla f(z) + \nabla^2 f(\xi)(x - z)$ . Therefore,

$$\|\nabla f(x) - \nabla f(z)\|_2 \leq \max_{\xi \in \mathcal{X}} \|\nabla^2 f(\xi)\|_{op} \|x - z\|_2,$$

where  $\|\cdot\|_{op}$  denotes the operator norm. Since  $f$  is polynomial of order 4, the entries of  $\nabla^2 f$  are polynomials of order 2, and are thus bounded on the closed set  $\mathcal{X}$ . Therefore, the operator norm (magnitude of the largest eigenvalue of  $\nabla^2 f$ ) is bounded on  $\mathcal{X}$  due to the Gershgorin circle theorem. Denoting this finite value by  $C$ , we get that  $\nabla f(x)$  is  $C$ -Lipschitz on  $\mathcal{X}$ .  $\square$

Note that our convergence statement is only to a stationary point of the (implicit) objective,  $f + s$  and not to a global minimum. This is inevitable, as  $f$  is a nonconvex function. Extensions to backtracking line search, instead of fixed step size, can be adopted from [43], [44] as well.

#### B. Composition of convergence inducing operators

Unlike the projected MoM, in the projected EM the data-fidelity step is not a gradient step. It is well known that, on its own, the EM algorithm  $x_{k+1} = \mathcal{T}(x_k)$  converges to a local minimum of the negative log-likelihood function. However, to the best of our knowledge, the EM convergence behavior is not well understood, besides a few simple models. This motivates us to consider a framework of composition of two “black-box” operators that generate convergent sequences when being applied alone. Indeed, it is also known that the sequence  $x_{k+1} = \mathcal{D}(x_k)$ , under the convex proximity assumption of  $\mathcal{D}$ , converges to a minimizer of its associated  $s$  (e.g., as a special case of the proximal gradient method on  $0 + s$  [43], [44]). Furthermore, a gradient-step operator with sufficiently small step size on the MoM objective also yields a convergent sequence. Therefore, the analysis we provide for EM, may be also applicable to the MoM.

Denote by  $\text{Fix}(\mathcal{M})$  the set of fixed points of an operator  $\mathcal{M}$ , i.e.,  $\text{Fix}(\mathcal{M}) = \{x : \mathcal{M}(x) = x\}$ . As discussed above, both the data-fidelity operator  $\mathcal{T}$  and the denoising operator  $\mathcal{D}$  have fixed points associated with stationary points of a data-fidelity term  $f$  and an implicit prior term  $s$ , respectively.

Let us now define a class of operators that strictly attract points towards their set of fixed points, as has been used in [45].

**Definition IV.4.** We say that the map  $\mathcal{M} : \mathcal{X} \rightarrow \mathcal{X}$  is  $\gamma$ -strongly quasi-nonexpansive in  $\mathcal{X}$  with  $\gamma > 0$  if for all  $x \in \mathcal{X}$  and  $z \in \text{Fix}(\mathcal{M})$  we have

$$\|\mathcal{M}(x) - z\|_2^2 \leq \|x - z\|_2^2 - \gamma\|\mathcal{M}(x) - x\|_2^2.$$

Note that this class includes the set of proximal operators (see [45, Fact 1c]). Thus, it is a weaker assumption. Even though it is not guaranteed that the data-fidelity operator  $\mathcal{T}$  that is used in EM falls into this class for the entire domain, it might be reasonable to restrict the domain where it holds to be a small set  $\mathcal{X}$  around a fixed point. The following theorem shows how this property implies the convergence of the sequence  $x_{k+1} = \mathcal{D}(\mathcal{T}(x_k))$  to a fixed point.

**Theorem IV.5.** Let  $\mathcal{D} = \text{Prox}_s$  where  $s(\cdot)$  is a proper l.s.c. convex function with domain  $\mathcal{X}$ , and let  $\mathcal{T}$  be  $\gamma$ -strongly quasi-nonexpansive in  $\mathcal{X}$  such that  $\text{Fix}(\mathcal{D}) \cap \text{Fix}(\mathcal{T}) \neq \emptyset$ . Then, the sequence

$$x_{k+1} = \mathcal{D}(\mathcal{T}(x_k))$$

converges to a fixed point  $x_* = \mathcal{D}(\mathcal{T}(x_*))$ .

*Proof.* As a proximal operator associated with a convex function,  $\mathcal{D}$  is 1/2-average of a nonexpansive operator. Thus, from [45, Fact 1c], it is strongly quasi-nonexpansive. From [45, Prop. 1d] the composition of strongly quasi-nonexpansive operators  $\mathcal{M} = \mathcal{D} \circ \mathcal{T}$  with  $\text{Fix}(\mathcal{D}) \cap \text{Fix}(\mathcal{T})$  is strongly quasi-nonexpansive in  $\mathcal{X}$  with some  $\tilde{\gamma} > 0$  and  $\text{Fix}(\mathcal{M}) = \text{Fix}(\mathcal{D}) \cap \text{Fix}(\mathcal{T})$ . Let  $\tilde{x}_* \in \text{Fix}(\mathcal{M})$ , then

$$\|x_{k+1} - \tilde{x}_*\|_2^2 \leq \|x_k - \tilde{x}_*\|_2^2 - \tilde{\gamma}\|x_{k+1} - x_k\|_2^2.$$

Thus,

$$\|x_{k+1} - x_k\|_2^2 \leq \frac{1}{\tilde{\gamma}}(\|x_k - \tilde{x}_*\|_2^2 - \|x_{k+1} - \tilde{x}_*\|_2^2).$$

Summing over  $k$  from 0 to  $K$  we have

$$\begin{aligned} \sum_{i=1}^K \|x_{k+1} - x_k\|_2^2 &\leq \frac{1}{\tilde{\gamma}}(\|x_0 - \tilde{x}_*\|_2^2 - \|x_{K+1} - \tilde{x}_*\|_2^2) \\ &\leq \frac{1}{\tilde{\gamma}}\|x_0 - \tilde{x}_*\|_2^2 \end{aligned}$$

which implies  $\|x_{k+1} - x_k\|_2 \xrightarrow{K \rightarrow \infty} 0$ . Accordingly,  $x_k \rightarrow x_*$  that obeys  $x_* = \mathcal{D}(\mathcal{T}(x_*))$ .  $\square$

The above result, despite including assumptions that are not guaranteed for EM on the entire domain, provides

mathematical reasoning for the convergence of composition of a denoiser and a data-fitting operator, when each obeys convergence properties alone and both can agree on a fixed point (potentially, out of many fixed points that fit the measurements but can badly estimate the true signal). Note that the assumption  $\text{Fix}(\mathcal{D}) \cap \text{Fix}(\mathcal{T}) \neq \emptyset$  in the theorem is reasonable as we empirically show that the projected EM converges to a noiseless point that agrees with the measurements.

## V. NUMERICAL EXPERIMENTS

We proceed to examine the numerical performance of the proposed algorithms. For all experiments, we used the BM3D denoiser [40], where the noise level decays as in (III.1). Unless specified otherwise, we set  $F = 5$  for both algorithms. For MoM, we minimized the least squares objective (II.5) using the BFGS algorithm with line-search. The distributions  $\rho_1, \rho_2$  and their initial guesses were drawn from a uniform distribution on  $[0, 1]$ , and normalized so that  $\rho_1, \rho_2 \in \Delta^{L_{\text{high}}}$ . The pixel values of all images are in  $[0, 1]$ . Each pixel in the initialization of the image estimate, for both algorithms, was drawn i.i.d. from a uniform distribution on  $[0, 1]$ , which was then normalized to include the entire  $[0, 1]$  range.

Despite the non-convexity of EM and MoM, we observed that a single random initial guess provides consistent results, which are not significantly improved when adding more initial guesses.

To account for the shift-invariance of (I.1), we measure the error by:

$$\text{error}(\hat{x}) = \min_s \frac{\|R_s \hat{x} - x\|_F}{\|x\|_F}, \quad (\text{V.1})$$

where  $\hat{x}$  is the estimated image, and  $R_s$  denotes a 2D translation. We define SNR as

$$\text{SNR} = \frac{\|x\|_F^2}{L_{\text{high}}^2 \sigma^2}. \quad (\text{V.2})$$

Our algorithms were implemented in Torch. The recovery of a high-dimensional signal requires an efficient implementation of the algorithms over GPU. Actually, without this implementation, we were unable to recover images of size  $L_{\text{high}} \geq 32$  within a reasonable running time, where reducing the resolution beyond that adversely affects denoising performance. The code to reproduce all experiments is available at [https://github.com/JonathanShani/Denoiser\\_projection](https://github.com/JonathanShani/Denoiser_projection).

### A. Performance comparison

This section compares the performance of the projected MoM of Algorithm (1) and the projected EM

of Algorithm (2). We applied the algorithms to the 68 "natural" images of the CBSD-68 dataset and to a cryo-EM image of the E. coli 70S ribosome, available at the Electron Microscopy Data Bank [1]. We set  $L_{\text{high}} = 128$ , and the images were down-sampled to  $L_{\text{low}} = 64, 32, 16, 8$  (namely, down-sampling factors of  $K = 2, 4, 6, 8$ , respectively).

1) *Visual examples*: Figure 3 presents a collection of visual recoveries from the CBSD-68 dataset using both algorithms, with a down-sampling factor of  $K = 2$ . For the projected MoM, we assumed to have access to the population (exact) moments (which is the case when  $N \gg \sigma^4$ ), and the projected EM used  $N = 10^4$  observations with noise level of  $\sigma = 1/8$  (corresponding to  $\text{SNR} \approx 15$ ). Clearly, the projected EM provides more accurate recoveries, although MoM uses exact moments. However, as we show next, the computational load of the projected EM is much heavier.

2) *Comprehensive comparison*: We conducted a systematic comparison between the projected EM algorithm and the projected MoM in terms of estimation error and running time. While the reported running times should be taken with a grain of salt as they depend on implementation and hardware, our goal here is to show the general behavior of the algorithms.

Table I presents the error and running time, averaged over 20 trials. We used the Lena image of size  $L_{\text{high}} = 128$  with down-sampling factors of  $K = 4, 8$ , and of size  $L_{\text{high}} = 64$  with  $K = 2$ ; the number of observations was set to  $N = 10^2, 10^4$ , and the noise level to  $\sigma = 0.125, 0.25, 0.5$  (corresponding to  $\text{SNR} \approx 17, 4, 1$ , respectively). Both algorithms were limited to 100 iterations per trial. For each trial, we drew a fresh set of observations based on a new distribution and initial guesses. The projected EM shows a clear advantage for almost all values of  $N$  and  $\sigma$  in terms of estimation error (besides some cases when  $\sigma$  is large and  $N$  is small). However, the computational burden of EM is much heavier; there are cases (e.g.,  $L_{\text{high}} = 128, N = 10^4, \sigma = 0.25$ ) where the running time of the projected EM algorithm is 30 times longer than the running time of the projected MoM. The reason is that EM iterates over all observations, whereas MoM requires only a single pass over the observations [46], while the dimension of the variables in the least squares objective (II.9) is proportional to the dimension of the image.

3) *Error as a function of the iterations*: We next examined the behavior of the algorithms as a function of their iterations, averaged over all images in the CBSD-68 dataset of size  $L_{\text{high}} = 128$ . The projected MoM used exact moments, and the projected EM used  $N = 10^4$  observations and noise level of  $\sigma = 1/8$ .

The results, for a variety of sampling factors, are presented in Figure 4. As can be seen, the algorithms with projections significantly outperform the unprojected versions for all down-sampling factors. Notably, the projected algorithms provide non-trivial estimates even for  $K = 16$  (when each measurement is down-sampled from  $128 \times 128$  to  $8 \times 8$ ). We note that the denoiser leads to locally non-monotonic error curves.

The following section presents more visual results of the projected EM algorithm. The experiments in Sections V-C, V-D and V-E study the influence of different parameters on performance. These experiments require averaging over multiple trials, which makes it virtually impossible to produce results for EM in a reasonable running time. For that reason, these experiments were only conducted for MoM. In addition, we also tested the Plug-and-Play approach as described in Section II-D, where the minimization function  $l(\theta)$  is based on moment matching. However, we were unable to find any pair of parameters  $(\lambda, \beta)$  that provided satisfactory results across a variety of images.

### B. Visual examples of the projected EM algorithm

Figure 5 presents recoveries of the images presented in Figure 1, using the projected EM algorithm with sampling factors of  $K = 2, 4, 8$ ,  $N = 10^4$  observations and noise level of  $\sigma = 1/8$ . It is quite remarkable that the projected EM provides accurate estimates with  $K = 8$ , namely, when the number of pixels is reduced from  $128^2$  to  $16^2$ : a factor of 64.

### C. Projected MoM performance as a function of SNR

Figure 6 shows the average recovery error of the projected MoM algorithm as a function of the SNR. All experiments were conducted with the Lena image of size  $L_{\text{high}} = 32$ , with a sampling factor of  $K = 2$ , and  $N = 10^5$  observations. For each SNR value, we conducted 100 trials, each with a fresh distribution of translations. As can be seen, the error decreases monotonically with the SNR. Remarkably, the slope of the curve increases as the SNR decreases, hinting that the sample complexity of the problem (the number of observations required to achieve a desired accuracy) increases in the low SNR regime; this is a known phenomenon in the MRA literature for models with no projection; see for example [5]–[7].

### D. Projected MoM performance as a function of the number of measurements

By the law of large numbers and according to (II.4), for any fixed SNR, the empirical moments almost surely

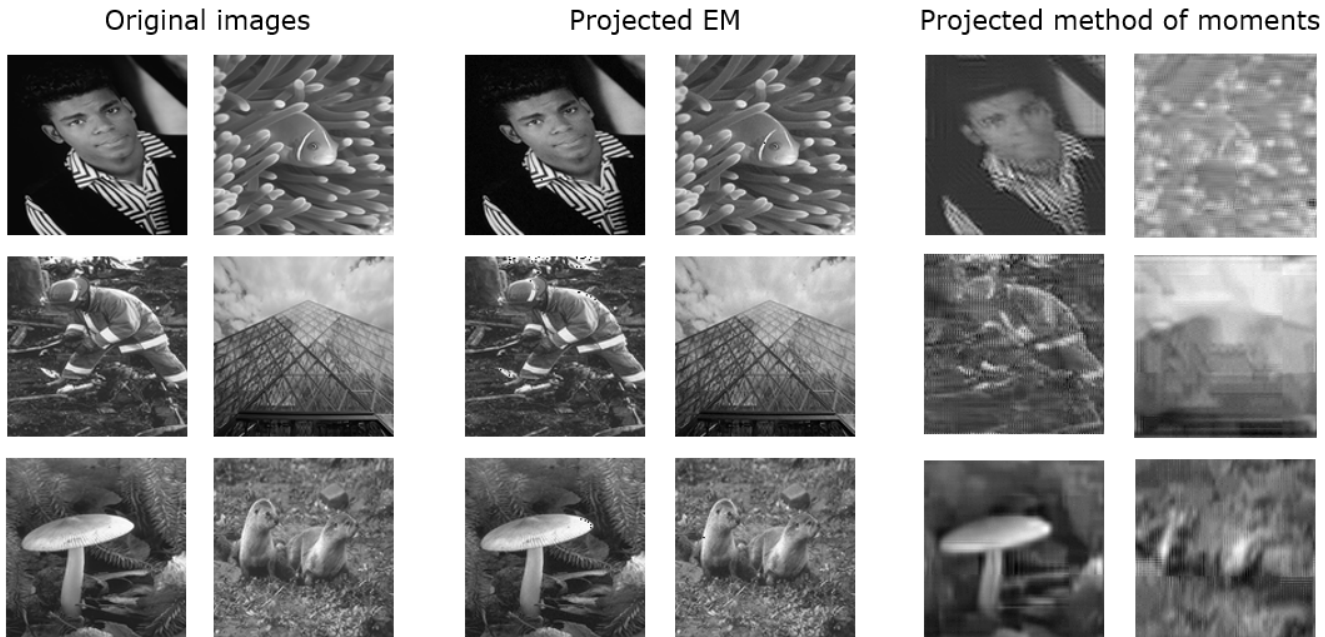


Fig. 3. A gallery of 6 examples from the CBSD-68 dataset, and the corresponding recoveries using projected EM in a high-SNR regime ( $\sigma = 1/8$ ) and projected MoM with accurate moments ( $N \gg \sigma^4$ ); the images were down-sampled by a factor of  $K = 2$ . It can be seen that the projected EM outperforms the projected MoM. However, as we show in Table I, the computational load of the projected EM algorithm is much heavier.

converge to the analytic moments. To assess the impact of the number of observations on the estimation error, we used the image of Lena of size  $L_{\text{high}} = 32$ , down-sampling factor of  $K = 2$ , and noise level of  $1/8$ , corresponding to  $\text{SNR} \approx 17$ .

Figure 7 presents the average error, over 100 trials, as a function of  $N$ . For each trial, we drew a fresh distribution. The error indeed decreases with  $N$ , as expected, but the slope is smaller than  $-1/2$  (in logarithmic scale), as the law of large numbers predicts. This is due to the effect of the prior (manifested as a denoiser in our case), which does not depend on the observations (the data).

#### E. How frequently should we apply the denoiser?

An important parameter of the proposed algorithms, denoted by  $F$ , determines after how many gradient steps (or EM iterations for the projected EM algorithm) we apply the denoiser. For example,  $F = 1$  means that we apply the denoiser after each gradient step, whereas  $F = 100$  means that we run 100 gradient steps before applying the denoiser. This is especially important since the computational complexity of a single gradient step is significantly heavier than a BM3D application. To study the effect of this parameter for the projected MoM, we used the image of Lena of size  $L_{\text{high}} = 128$ , down-sampling factor of  $K = 2$ , and assumed to have access to the population (perfect) moments.

Figure 8 shows the average error (over 10 trials) of MoM for different values of  $F$ ; each trial was conducted with a fresh distribution. Plainly, the impact of  $F$  on the performance is significant. The optimal value seems to be around  $F = 10$  in this case; larger and smaller values of  $F$  lead to sub-optimal results.

## VI. POTENTIAL IMPLICATIONS FOR CRYO-EM

Single-particle cryo-EM is an increasingly popular technology for high resolution structure determination of biological molecules, and in particular proteins [9]. The cryo-EM reconstruction problem is to estimate a 3-D structure (the electric potential map of the molecule of interest) from multiple observations of the form

$$y = TR_{\omega}X + \varepsilon, \quad (\text{VI.1})$$

where  $X$  is the 3-D structure to be recovered,  $R_{\omega}$  represents an unknown 3-D rotation by some angle  $\omega \in SO(3)$ , and  $T$  is a fixed, linear tomographic projection. The noise level is typically very high. The SR-MRA problem (I.1) can be interpreted as a toy model of the cryo-EM problem, where the image plays the role of the 3-D structure, and the 2D translations and the sampling operator  $P$  replace, respectively, the unknown 3-D rotations and the tomographic projection.

The standard reconstruction algorithms in cryo-EM are based on EM [37], [38], aiming to maximize the

TABLE I

COMPARISON BETWEEN THE PROJECTED MoM AND PROJECTED EM FOR A VARIETY OF MODELS (DETERMINED BY THE TARGET RESOLUTION  $L_{\text{HIGH}}$  AND THE OBSERVED RESOLUTION  $L_{\text{LOW}}$ ), NUMBER OF OBSERVATIONS  $N$ , AND NOISE LEVEL  $\sigma$ .

Model parameters				Projected MoM		Projected EM	
$L_{\text{high}}$	$L_{\text{low}}$	$N$	$\sigma$	Error	Time	Error	Time
128	32	100	0.125	0.332	<b>266.5421</b>	<b>0.0991</b>	871.6759
128	32	100	0.25	0.3459	<b>207.2537</b>	<b>0.196</b>	861.4668
128	32	100	0.5	<b>0.356</b>	<b>120.2959</b>	0.3836	837.9343
128	32	10000	0.125	0.339	<b>261.8394</b>	<b>0.0311</b>	1593.9534
128	32	10000	0.25	0.3302	<b>280.6154</b>	<b>0.0623</b>	1668.756
128	32	10000	0.5	0.3301	<b>277.3122</b>	<b>0.1387</b>	1660.7012
128	16	100	0.125	0.3627	<b>85.716</b>	<b>0.2475</b>	919.5462
128	16	100	0.25	<b>0.411</b>	<b>84.4553</b>	0.4154	984.6871
128	16	100	0.5	<b>0.3714</b>	<b>77.8746</b>	0.7497	893.2808
128	16	10000	0.125	0.3874	<b>122.5611</b>	<b>0.0685</b>	3769.9855
128	16	10000	0.25	0.381	<b>113.7814</b>	<b>0.141</b>	3179.0298
128	16	10000	0.5	0.3652	<b>94.8278</b>	<b>0.3001</b>	3148.3869
64	32	100	0.125	0.3319	103.8799	<b>0.0494</b>	<b>100.9239</b>
64	32	100	0.25	0.3427	<b>47.959</b>	<b>0.0988</b>	99.215
64	32	100	0.5	0.3439	<b>44.0597</b>	<b>0.2111</b>	87.1056
64	32	10000	0.125	0.2562	<b>101.4311</b>	<b>0.0158</b>	325.7816
64	32	10000	0.25	0.3382	<b>100.1693</b>	<b>0.0315</b>	264.8022
64	32	10000	0.5	0.3349	<b>98.7658</b>	<b>0.0647</b>	276.1571

posterior distribution based on analytical, explicit priors. Recently, techniques based on MoM were also designed for quick ab initio modeling [47], [48]. The techniques proposed in this paper can be readily integrated into these schemes, which may lead to improved accuracy and acceleration. A similar idea was recently suggested by [49], who used the regularization by denoising technique [19], and showed recoveries of moderate resolution with simulated data.

Current cryo-EM technology cannot be used to reconstruct small molecular structure (below  $\sim 40$  kDa): this is one of its main drawbacks [50]. Recent papers suggested overcoming this barrier using variations of the MoM and EM [51], [52]. However, as the problem is ill-conditioned, the resolution of the recovered structures is not high enough. We hope that modifications of the algorithms suggested in this paper, where the denoiser is replaced with a data-driven projection operator, can be used to increase the resolution of the reconstructions, and thus will allow elucidating multiple new structures of small biological molecules.

## REFERENCES

- [1] <https://www.ebi.ac.uk/emdb/>, 2, 9
- [2] T. Bendory, A. Jaffe, W. Leeb, N. Sharon, and A. Singer, "Super-resolution multi-reference alignment," *Information and Inference: A Journal of the IMA*, vol. 11, no. 2, pp. 533–555, 2022. 1, 3
- [3] A. S. Bandeira, Y. Chen, R. R. Lederman, and A. Singer, "Non-unique games over compact groups and orientation estimation in cryo-EM," *Inverse Problems*, vol. 36, no. 6, 2020. 1
- [4] A. S. Bandeira, B. Blum-Smith, J. Kileel, A. Perry, J. Weed, and A. S. Wein, "Estimation under group actions: recovering orbits from invariants," *arXiv preprint arXiv:1712.10163*, 2017. 1
- [5] T. Bendory, N. Boumal, C. Ma, Z. Zhao, and A. Singer, "Bispectrum inversion with application to multireference alignment," *IEEE Transactions on Signal Processing*, vol. 66, no. 4, pp. 1037–1050, 2017. 1, 9
- [6] E. Abbe, T. Bendory, W. Leeb, J. M. Pereira, N. Sharon, and A. Singer, "Multireference alignment is easier with an aperiodic translation distribution," *IEEE Transactions on Information Theory*, vol. 65, no. 6, pp. 3565–3584, 2018. 1, 4, 9
- [7] A. Perry, J. Weed, A. S. Bandeira, P. Rigollet, and A. Singer, "The sample complexity of multireference alignment," *SIAM Journal on Mathematics of Data Science*, vol. 1, no. 3, pp. 497–517, 2019. 1, 9
- [8] T. Bendory, D. Edidin, W. Leeb, and N. Sharon, "Dihedral multi-reference alignment," *IEEE Transactions on Information Theory*, vol. 68, no. 5, pp. 3489–3499, 2022. 1
- [9] T. Bendory, A. Bartesaghi, and A. Singer, "Single-particle cryo-electron microscopy: Mathematical theory, computational challenges, and opportunities," *IEEE Signal Processing Magazine*, vol. 37, no. 2, pp. 58–76, 2020. 1, 10
- [10] W. Park, C. R. Midgett, D. R. Madden, and G. S. Chirikjian, "A stochastic kinematic model of class averaging in single-particle electron microscopy," *The International journal of robotics research*, vol. 30, no. 6, pp. 730–754, 2011. 1
- [11] S. H. Scheres, M. Valle, R. Nuñez, C. O. Sorzano, R. Marabini, G. T. Herman, and J.-M. Carazo, "Maximum-likelihood multi-reference refinement for electron microscopy images," *Journal of molecular biology*, vol. 348, no. 1, pp. 139–149, 2005. 1
- [12] D. M. Rosen, L. Carlone, A. S. Bandeira, and J. J. Leonard, "A certifiably correct algorithm for synchronization over the special Euclidean group," in *Algorithmic Foundations of Robotics XII*. Springer, 2020, pp. 64–79. 1
- [13] J. P. Zwart, R. van der Heiden, S. Gelsema, and F. Groen, "Fast translation invariant classification of hrr range profiles in a zero phase representation," *IEE Proceedings-Radar, Sonar and Navigation*, vol. 150, no. 6, pp. 411–418, 2003. 1

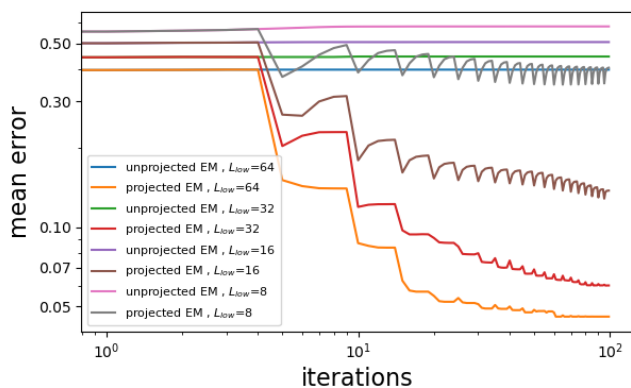
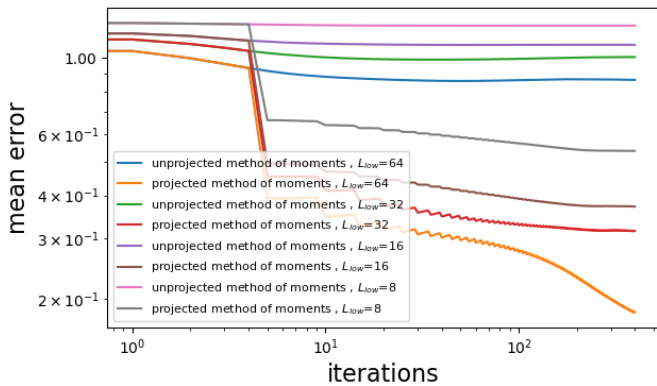


Fig. 4. Error as a function of the iteration (averaged over all images in the CBSD-68 dataset, each of size  $L_{\text{high}} = 128$ ), for different sampling factors. The upper panel presents the projected MoM and the unprojected MoM, based on the perfect moments (corresponding to  $N \rightarrow \infty$ ). The lower panel presents the projected and unprojected EM, with  $N = 10^4$  observations and noise level of  $\sigma = 1/8$ .

- [14] R. Gil-Pita, M. Rosa-Zurera, P. Jarabo-Amores, and F. López-Ferreras, “Using multilayer perceptrons to align high range resolution radar signals,” in *International Conference on Artificial Neural Networks*. Springer, 2005, pp. 911–916. 1
- [15] D. Robinson, S. Farsiu, and P. Milanfar, “Optimal registration of aliased images using variable projection with applications to super-resolution,” *The Computer Journal*, vol. 52, no. 1, pp. 31–42, 2009. 1
- [16] T. Bendory, I. Hadi, and N. Sharon, “Compactification of the rigid motions group in image processing,” *SIAM Journal on Imaging Sciences*, vol. 15, no. 3, pp. 1041–1078, 2022. 1
- [17] A. P. Dempster, N. M. Laird, and D. B. Rubin, “Maximum likelihood from incomplete data via the EM algorithm,” *Journal of the Royal Statistical Society: Series B (Methodological)*, vol. 39, no. 1, pp. 1–22, 1977. 1, 4
- [18] S. V. Venkatakrisnan, C. A. Bouman, and B. Wohlberg, “Plug-and-play priors for model based reconstruction,” in *2013 IEEE Global Conference on Signal and Information Processing*. IEEE, 2013, pp. 945–948. 2, 5
- [19] Y. Romano, M. Elad, and P. Milanfar, “The little engine that could: Regularization by denoising (red),” *SIAM Journal on Imaging Sciences*, vol. 10, no. 4, pp. 1804–1844, 2017. 2, 11



Fig. 5. Recoveries using the projected EM algorithm of the images presented in Figure 1, with noise level of  $\sigma = 1/8$  and  $N = 10^4$  observations. The down-sampling factors are  $K = 2$  (top row),  $K = 4$  (middle row), and  $K = 8$  (bottom row).

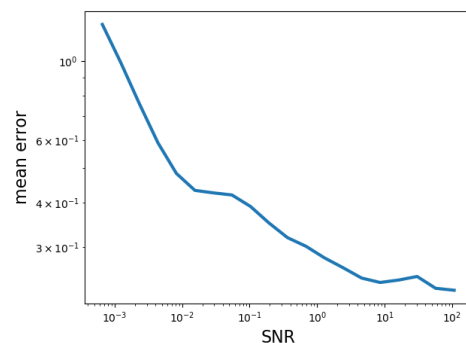


Fig. 6. Mean error of the projected MoM as a function of the SNR with  $N = 10^5$  observations. The experiments were conducted on an image of size  $L_{\text{high}} = 32$  with a down-sampling factor of  $K = 2$ . Remarkably, the slope of the curve increases as the SNR decreases, hinting that the sample complexity of the problem increases in the low SNR regime.

- [20] S. H. Chan, X. Wang, and O. A. Elgandy, “Plug-and-Play ADMM for image restoration: Fixed-point convergence and applications,” *IEEE Transactions on Computational Imaging*, vol. 3, no. 1, pp. 84–98, 2017. 2
- [21] K. Zhang, W. Zuo, S. Gu, and L. Zhang, “Learning deep cnn denoiser prior for image restoration,” in *Proceedings of the IEEE conference on computer vision and pattern recognition*, 2017, pp. 3929–3938. 2
- [22] T. Ttirer and R. Giryes, “Image restoration by iterative denoising and backward projections,” *IEEE Transactions on Image Processing*, vol. 28, no. 3, pp. 1220–1234, 2018. 2
- [23] —, “Super-resolution via image-adapted denoising CNNs: Incorporating external and internal learning,” *IEEE Signal Processing Letters*, vol. 26, no. 7, pp. 1080–1084, 2019. 2
- [24] K. Zhang, Y. Li, W. Zuo, L. Zhang, L. Van Gool, and R. Timofte, “Plug-and-play image restoration with deep denoiser prior,” *IEEE Transactions on Pattern Analysis and Machine Intelligence*, 2021. 2
- [25] E. Ryu, J. Liu, S. Wang, X. Chen, Z. Wang, and W. Yin, “Plug-and-play methods provably converge with properly trained denoisers,” in *International Conference on Machine Learning*, vol. 97, 09–15 Jun 2019, pp. 5546–5557. 2
- [26] A. Rond, R. Giryes, and M. Elad, “Poisson inverse problems by

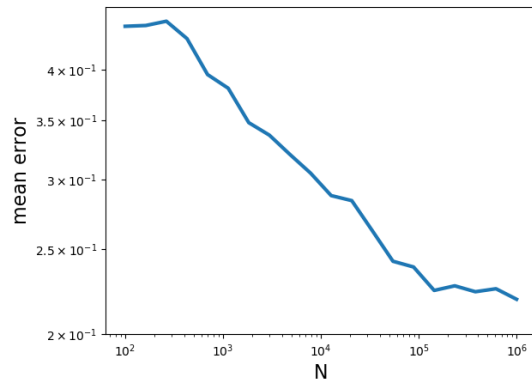


Fig. 7. Mean error of the projected MoM as a function of the number of observations  $N$ . The experiments were conducted on an image of size  $L_{\text{high}} = 32$  with a down-sampling factor of  $K = 2$  and noise level of  $\sigma = 1/8$ .

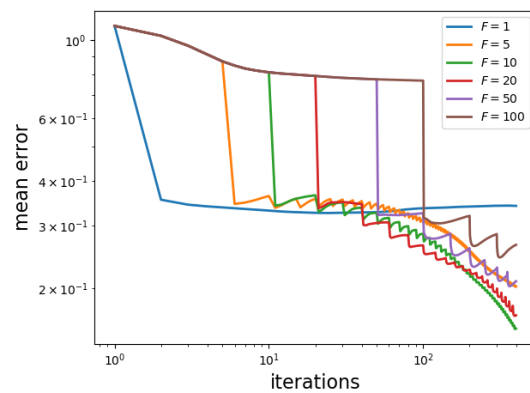


Fig. 8. Mean error of the projected MoM as a function of the iteration, for different values of  $F$  (number of gradient steps between consecutive denoising operations). The experiments were conducted on an image of size  $L_{\text{high}} = 128$ , assuming to have access to the population moments, and with a down-sampling factor of  $K = 2$ . The optimal value seems to be around  $F = 10$ ; larger and smaller values of  $F$  lead to sub-optimal results.

the Plug-and-Play scheme,” *Journal of Visual Communication and Image Representation*, vol. 41, pp. 96–108, 2016. 2

- [27] Y. Dar, A. M. Bruckstein, M. Elad, and R. Giryes, “Postprocessing of compressed images via sequential denoising,” *IEEE Transactions on Image Processing*, vol. 25, no. 7, pp. 3044–3058, 2016. 2
- [28] U. S. Kamilov, H. Mansour, and B. Wohlberg, “A plug-and-play priors approach for solving nonlinear imaging inverse problems,” *IEEE Signal Processing Letters*, vol. 24, no. 12, pp. 1872–1876, 2017. 2
- [29] K. Wei, A. Aviles-Rivero, J. Liang, Y. Fu, C.-B. Schönlieb, and H. Huang, “Tuning-free plug-and-play proximal algorithm for inverse imaging problems,” in *International Conference on Machine Learning*. PMLR, 2020, pp. 10 158–10 169. 2
- [30] T. Meinhardt, M. Moller, C. Hazirbas, and D. Cremers, “Learning proximal operators: Using denoising networks for regularizing inverse imaging problems,” in *Proceedings of the IEEE International Conference on Computer Vision*, 2017. 2
- [31] G. T. Buzzard, S. H. Chan, S. Sreehari, and C. A. Bouman, “Plug-and-play unplugged: Optimization-free reconstruction using consensus equilibrium,” *SIAM Journal on Imaging Sciences*, vol. 11, no. 3, pp. 2001–2020, 2018. 2
- [32] Y. Sun, B. Wohlberg, and U. S. Kamilov, “An online plug-and-play algorithm for regularized image reconstruction,” *IEEE Transactions on Computational Imaging*, 2019. 2
- [33] E. T. Reehorst and P. Schniter, “Regularization by denoising: Clarifications and new interpretations,” *IEEE Transactions on Computational Imaging*, vol. 5, no. 1, pp. 52–67, 2019. 2
- [34] E. Yogev-Ofer, T. Tirer, and R. Giryes, “An interpretation of regularization by denoising and its application with the back-projected fidelity term,” in *2021 IEEE International Conference on Image Processing (ICIP)*. IEEE, 2021, pp. 1649–1653. 2
- [35] S. Abu-Hussein, T. Tirer, S. Y. Chun, Y. C. Eldar, and R. Giryes, “Image restoration by deep projected gsure,” in *Proceedings of the IEEE/CVF Winter Conference on Applications of Computer Vision*, 2022, pp. 3602–3611. 2
- [36] A. Abas, T. Bendory, and N. Sharon, “The generalized method of moments for multi-reference alignment,” *IEEE Transactions on Signal Processing*, vol. 70, pp. 1377–1388, 2022. 3, 4
- [37] A. Punjani, J. L. Rubinstein, D. J. Fleet, and M. A. Brubaker, “cryoSPARC: algorithms for rapid unsupervised cryo-EM structure determination,” *Nature methods*, vol. 14, no. 3, pp. 290–296, 2017. 4, 10
- [38] S. H. Scheres, “RELION: implementation of a bayesian approach to cryo-EM structure determination,” *Journal of structural biology*, vol. 180, no. 3, pp. 519–530, 2012. 4, 10
- [39] N. Janco and T. Bendory, “An accelerated expectation-maximization algorithm for multi-reference alignment,” *IEEE Transactions on Signal Processing*, vol. 70, pp. 3237–3248, 2022. 5
- [40] K. Dabov, A. Foi, V. Katkovnik, and K. Egiazarian, “Image denoising by sparse 3-D transform-domain collaborative filtering,” *IEEE Transactions on image processing*, vol. 16, no. 8, pp. 2080–2095, 2007. 6, 8
- [41] J.-J. Moreau, “Proximité et dualité dans un espace hilbertien,” *Bull. Soc. Math. France*, vol. 93, no. 2, pp. 273–299, 1965. 7
- [42] R. Gribonval and M. Nikolova, “A characterization of proximity operators,” *Journal of Mathematical Imaging and Vision*, vol. 62, no. 6, pp. 773–789, 2020. 7
- [43] A. Beck and M. Teboulle, “Gradient-based algorithms with applications to signal recovery,” *Convex optimization in signal processing and communications*, pp. 42–88, 2009. 7
- [44] A. Beck, *First-order methods in optimization*. SIAM, 2017. 7
- [45] I. Yamada and N. Ogura, “Hybrid steepest descent method for variational inequality problem over the fixed point set of certain quasi-nonexpansive mappings,” 2005. 8
- [46] N. Boumal, T. Bendory, R. R. Lederman, and A. Singer, “Heterogeneous multireference alignment: A single pass approach,” in *2018 52nd Annual Conference on Information Sciences and Systems (CISS)*. IEEE, 2018, pp. 1–6. 9
- [47] E. Levin, T. Bendory, N. Boumal, J. Kileel, and A. Singer, “3D ab initio modeling in cryo-EM by autocorrelation analysis,” in *2018 IEEE 15th International Symposium on Biomedical Imaging (ISBI 2018)*. IEEE, 2018, pp. 1569–1573. 11
- [48] N. Sharon, J. Kileel, Y. Khoo, B. Landa, and A. Singer, “Method of moments for 3D single particle ab initio modeling with non-uniform distribution of viewing angles,” *Inverse Problems*, vol. 36, no. 4, p. 044003, 2020. 11
- [49] D. Kimanius, G. Zickert, T. Nakane, J. Adler, S. Lunz, C.-B. Schönlieb, O. Öktem, and S. H. Scheres, “Exploiting prior knowledge about biological macromolecules in cryo-EM structure determination,” *IUCrJ*, vol. 8, no. 1, 2021. 11
- [50] R. Henderson, “The potential and limitations of neutrons, electrons and X-rays for atomic resolution microscopy of unstained biological molecules,” *Quarterly reviews of biophysics*, vol. 28, no. 2, pp. 171–193, 1995. 11
- [51] T. Bendory, N. Boumal, W. Leeb, E. Levin, and A. Singer, “Toward single particle reconstruction without particle picking:

Breaking the detection limit,” *arXiv preprint arXiv:1810.00226*, 2018. 11

- [52] S. Kreymer, A. Singer, and T. Bendory, “A stochastic approximate expectation-maximization for structure determination directly from cryo-EM micrographs,” *arXiv preprint arXiv:2303.02157*, 2023. 11